processes

MDPI

Article

Numerical Simulation of Casing Failure Induced by Mudstone Hydration: Strain Evolution and Localization Pattern

Kun Zhu [1], Fanshun Meng [1,*], Tianyu Yi [1], Zhanyuan Liang [2], Xiaoyu Zhang [2] and Tao Jiang [3]

[1] College of Marine Geosciences, Ocean University of China, Qingdao 266100, China; zhukun@stu.ouc.edu.cn (K.Z.); ymeric@sina.com (T.Y.)
[2] Institute of Oceanographic Instrumentation, Qilu University of Technology (Shandong Academy of Sciences), Qingdao 266001, China; lzy09017216@163.com (Z.L.); zhxy_upc@126.com (X.Z.)
[3] Information Research Department, Qingdao National Laboratory for Marine Science and Technology, Qingdao 266237, China; tjiang@qnlm.ac
* Correspondence: mengfsh@ouc.edu.cn; Tel.: +86-13953227028

Abstract

Mudstone hydration is a critical factor contributing to casing failure during water injection operations in oilfield development. However, the relationship between hydration-induced stress evolution and casing failure mechanisms remains insufficiently understood. In this study, a three-dimensional fluid–solid coupling numerical model of the casing–cement sheath-formation system was developed, based on the nonlinear correlation between mudstone water content and its mechanical properties. Experiment results indicate that increasing the water content from 2% to 8% reduces the shear strength of mudstone by 89.7%. The axial shear strain distribution along the casing exhibits a pattern of lowvalues in the central section and high values at both ends. With increasing water content, the shear strain response evolves through three stages: weak localization at 2–3%, enhanced localization at 4–5%, and pronounced ring-shaped localization at 8%. Furthermore, localization analysis identifies lithological interfaces as high-risk zones, where strain gradient reversals occur within both the cement sheath and casing. By integrating simulation with observed casing failure data, this study elucidates the progression of casing failure mechanisms in the studied oilfield, providing a mechanistic basis for identifying and mitigating casing failure in waterflood-developed oilfields with extensive mudstone intervals and complex geology.

Keywords: casing failure; mudstone hydration; water content; strain evolution; localization analysis

1. Introduction

Casing failure has become a persistent technical challenge in the prolonged development of oilfields, particularly under complex geological conditions where multi-physical field interactions give rise to highly nonlinear failure mechanisms. Among these factors, mudstone hydration is widely recognized as a primary contributor to casing deterioration. In waterflooded reservoirs, injected water inevitably invades adjacent mudstone layers, triggering a series of physicochemical processes that alter the rock's mechanical properties and volumetric stability. These changes impose abnormal loads on the casing, and if not properly understood, can lead to premature casing failure and compromised well integrity. Therefore, a quantitative understanding of how mudstone hydration affects casing integrity is essential for efficient and safe oilfield development throughout its operational lifespan.

Check for updates

Received: 9 May 2026
Revised: 24 June 2026
Accepted: 27 June 2026
Published: 30 June 2026

Copyright: © 2026 by the authors. Licensee MDPI, Basel, Switzerland. This article is an open access article distributed under the terms and conditions of the Creative Commons Attribution (CC BY) license.

Mechanical weakening and volumetric expansion are two primary coupled effects resulting from the interaction between water and mudstone. On one hand, water absorption reduces the uniaxial compressive strength and elastic modulus of mudstone in a nonlinear manner [1,2]. Nuclear magnetic resonance analyses further reveal that hydrolysis and ion exchange alter pore structures and promote microcrack propagation, leading to progressive macroscopic degradation [3]. On the other hand, expansive clay minerals such as montmorillonite adsorb water molecules into their interlayer spaces, generating swelling pressure that can reach substantial magnitudes [4,5]. These two effects are not independent. Swelling-induced microcracks facilitate deeper water infiltration, which further weakens the rock, while reduced mechanical strength limits the rock's resistance to expansion, creating a positive feedback loop that accelerates material deterioration [6,7].

Hydration-induced coupling effects in mudstone often present significant challenges in oilfields with abundant mudstone deposits, where hydration reactions substantially affect the macroscopic mechanical properties and volumetric stability of the mudstone interval, thereby impacting the integrity of oilfield casing. Experimental studies have confirmed that water content has a dominant influence on mudstone strength [8] and that increased water content exacerbates internal failure [9]. Further mechanistic investigations have revealed that clay mineral expansion induces microcrack propagation and structural loosening, which primarily accounts for the degradation of mechanical properties in expansive mudstone [10]. Building upon this mechanistic understanding, a coupled model integrating humidity diffusion, deformation, and fracture processes has further elucidated the interaction mechanisms between moisture-induced swelling and creep deformation in mudstone [11]. On this basis, lateral expansion experiments have demonstrated that mudstone can develop substantial expansion strains [12], and that the resulting swelling pressure directly imposes additional radial stresses and generates stress concentration zones around the wellbore and casing [13]. Collectively, these findings indicate that mudstone hydration and creep are interrelated and mutually reinforcing phenomena. Their synergistic effects induce progressive displacement of the mudstone layer toward the wellbore, thereby imposing an increasingly non-uniform external load on the casing over time.

The mechanical behavior of the casing–cement sheath-formation system, which is central to oil and gas well integrity, has been progressively understood through a series of theoretical models. Early investigations treated the system as a three-layer thick-walled cylinder under axisymmetric loading, enabling determination of radial and hoop stress distributions using Lamé's equations [14]. To account for heterogeneous in situ stresses, subsequent work decomposed non-uniform ground stress into uniform and deviatoric components, yielding analytical solutions for the displacement field, stress field, and casing loads under non-uniform conditions [15]. Building on this decomposition, further refinements incorporated thermal and poroelastic effects by partitioning stresses into uniform, deviatoric, shear, and thermal components [16]. For wellbores with complex structural features, a semi-analytical technique combining elastic theory with the finite element method was developed to predict stress distributions around multilayer casings and cement sheaths [17]. In the specific context of localized mudstone swelling, the resulting axial non-uniform load was modeled as a parabolic distribution, and the stress function method was employed to obtain the casing stress distribution [18].

Building upon analytical models, numerical simulation techniques have been employed to further investigate the relationship between mudstone hydration and casing failure [19]. Finite element analyses on low-permeability reservoirs have demonstrated that the synergistic effect of non-uniform stress and mudstone creep is a primary mechanism driving casing failure [20]. Comparative studies across various loading zones have highlighted the predominant influence of load non-uniformity on casing deformation [21].

Moreover, both numerical simulations and experimental findings have revealed that even minimal amounts of water-sensitive minerals in mudstone can induce significant extrusion, bending, and shear deformation due to expansion along bedding planes [22], and that hydration-induced expansion of mud shale intensifies stress concentration at lithological interfaces, a critical factor contributing to casing deformation [23]. Recent studies have developed hydromechanical constitutive models for jointed rock masses based on compression–shear–seepage tests, in which shear–slip behavior, shear dilation, and hydraulic aperture evolution are coupled to describe seepage–deformation interaction [24]. These studies provide useful references for understanding seepage–deformation interaction in the aspect of intervals. However, most existing studies on casing failure still focus on mudstone swelling, non-uniform loading, or casing stress response, while the water content-dependent degradation of mudstone has rarely been quantitatively linked to shear strain evolution and localization in the casing–cement sheath-formation system. In particular, the strain transfer and localization behavior across the mudstone and marker interfaces under different water content conditions remain insufficiently clarified. Further investigation is needed to establish the intrinsic relationship between mudstone hydration, shear strain localization, and casing failure.

To address these challenges, this study focuses on the N_2 section in the southern Sartu Oilfield, Daqing, China. Based on core water absorption experimental data, a nonlinear correlation between mudstone water content and its mechanical properties is established. A three-dimensional hydro-mechanical coupled numerical model of the casing–cement sheath-formation system is developed to simulate the shear–strain response under different water content conditions. The analysis characterizes the evolution of shear strain at low, moderate, and high water content and quantifies the strain gradient changes across the mudstone and marker interfaces. These results clarify the transfer and localization of shear strain within the casing–cement sheath-formation system and provide a mechanistic basis for identifying casing failure positions in water-sensitive mudstone intervals.

2. Geological Background

The study area is located in the southern sector of the Sartu anticline, within the central depression of the northern Songliao Basin, Daqing, as shown in Figure 1. Within the Sartu structural domain, multiple faults have developed predominantly along northwest and west-northwest orientations. Seven major faults have been identified, each extending approximately 2900 m in length and exhibiting displacements exceeding 50 m [25]. In the study area, based on sedimentary epochs and source-reservoir-cap rock conditions, the N_2 section of the Nenjiang Formation can be classified as a cap rock interval. Of particular significance is the basal portion of the N_2 section, which contains oil shale intervals 5–15 m thick; these intervals serve as marker stratigraphic markers with substantial regional correlation value. This marker layer is characterized by well-developed horizontal bedding, flanked above and below by mudstone layers enriched in clay minerals.

Three-dimensional seismic structural interpretation reveals that the orientations of the major faults generally correspond with those identified previously, although some faults have experienced lateral extension. Evidence indicates fault intersections and potential changes in direction. Most newly identified small faults intersect with primary and secondary faults, resulting in the formation of multiple closed and semi-closed small fault blocks. Within these blocks, secondary development of minor faults with relatively limited extension lengths has occurred. The distribution of numerous small-scale faults within these blocks contributes to highly complex oil–water connectivity throughout the entire structural framework.

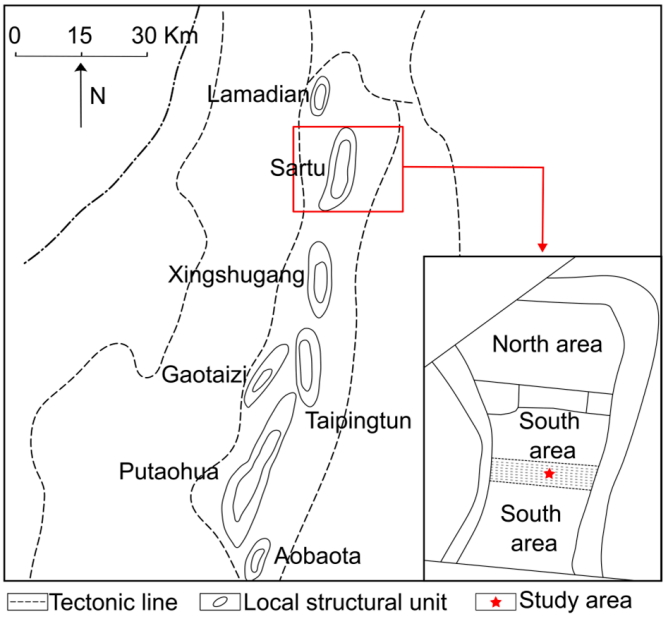


Figure 1. Geological map of study area in Sartu Oilfield.

The southern Sartu Oilfield is characterized by long-term water injection, complex fault-block structures, water-sensitive mudstone intervals, and abundant records of casing failure. These geological and development conditions make it a suitable field case for investigating hydration-induced casing failure.

3. Methodology

A sequential one-way fluid–solid coupling approach was employed. The seepage field was first computed using the Richards equation based on mass conservation and Darcy's law, and the resulting water content distribution was subsequently incorporated into the mechanical model. Deformation-induced changes in pore structure and hydraulic conductivity caused by solid deformation were not fed back into the seepage analysis [26]. The migration of injected water can be described by the Richards equation based on mass conservation and Darcy's law. If the pressure head is denoted as h, the seepage process can be expressed as:

$$C(h)\frac{\partial h}{\partial t} = \nabla \cdot [K(h)\nabla(h+z)] \tag{1}$$

where, $C(h) = \frac{d\omega}{dh}$ is the specific water capacity, representing the change in water content per unit change in pressure head h; $K(h) = K_s k_r(h)$ is the unsaturated hydraulic conductivity; K_s is saturated hydraulic conductivity, m/s; $k_r(h)$ is relative permeability; z is elevation head (positive upward), m.

If $h < 0$ is defined as the unsaturated seepage zone and $h \geq 0$ as the saturated seepage zone, then based on the van Genuchten–Mualem model [27], the soil–water characteristic relationship for this region can be expressed as:

$$\omega(h) = \begin{cases} \omega_r + \frac{\omega_s - \omega_r}{\left[1+|ah|^n\right]^{1-\frac{1}{n}}} & ,h < 0 \\ \omega_s & ,h \geq 0 \end{cases} \tag{2}$$

where $\omega(h)$ is volumetric water content; ω_s is saturated water content; ω_r is residual water content; α is related to the reciprocal of the air-entry value, m^{-1}; n is pore-size distribution index.

The relative permeability relationship can be expressed as:

$$k_r(h) = \begin{cases} \left[1 - (\alpha|h|)^{n-1}\left(1 + (\alpha|h|)^n\right)^{\frac{1}{n}-1}\right]^2 & ,h < 0 \\ 1 & ,h \geq 0 \end{cases} \quad (3)$$

During the calculation process, Equation (2) determines the update matrix for the time step, and Equation (3) determines the magnitude of the water flow velocity. By simultaneously solving the above equations iteratively, the distribution of pressure head $h(x,t)$ is obtained. The van Genuchten soil–water characteristic curve described by Equation (2) can convert the pressure head into the spatiotemporal distribution of water content $\omega(x,t)$.

Under the assumption of plane strain and axisymmetric loading, the radial displacement and stress distributions in the casing–cement sheath-formation system follow the classical Lamé solution for thick-walled cylinders [28]. For the casing–cement sheath-formation model, as shown in Figure 2, given inner radius of the casing as r_1 and outer radius as r_2, the stress distribution and displacement expressions inside the casing can be obtained, which can be written as:

$$\begin{cases} \sigma_{rc}(r) = \frac{p_i {r_1}^2 - p_c {r_2}^2}{{r_2}^2 - {r_1}^2} - \frac{p_i - p_c}{{r_2}^2 - {r_1}^2}\frac{{r_1}^2 {r_2}^2}{r^2} \\ \sigma_{\theta c}(r) = \frac{p_i {r_1}^2 - p_c {r_2}^2}{{r_2}^2 - {r_1}^2} + \frac{p_i - p_c}{{r_2}^2 - {r_1}^2}\frac{{r_1}^2 {r_2}^2}{r^2} \end{cases} \quad (4)$$

$$u_c(r) = \frac{1 + \nu_c}{E_c}\left(-\frac{{r_1}^2 {r_2}^2}{r}\frac{p_c - p_i}{{r_2}^2 - {r_1}^2} + \frac{p_i {r_1}^2 - p_c {r_2}^2}{{r_2}^2 - {r_1}^2} r(1 - 2\nu_c)\right) \quad (5)$$

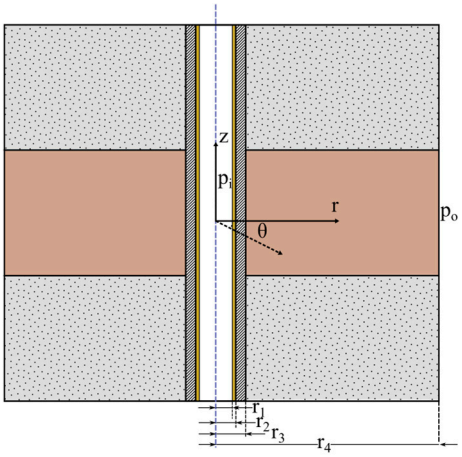


Figure 2. Schematic diagram of the axial geometric model of the casing.

Similarly, the radial stress distribution and radial displacement of the cement sheath and the formation can be determined sequentially. Given the internal pressure p_i and external pressure p_o acting on the system, the external pressure p_c on the casing can be determined from the continuity conditions, and then the radial displacement of the casing can be calculated. The elastic solution for thick-walled cylinders presented in this section provides the basic theoretical framework for subsequent numerical simulations, which is used to understand the stress distribution laws under axisymmetric loading.

4. Numerical Model and Data

To quantitatively investigate the influence of mudstone hydration on casing shear deformation during water injection operations, a three-dimensional numerical model was developed. This model incorporates factors such as water injection pressure, mudstone

water content, and the degradation of mechanical properties, and is based on the simulation framework of the casing–cement sheath-formation system, as illustrated in Figure 3.

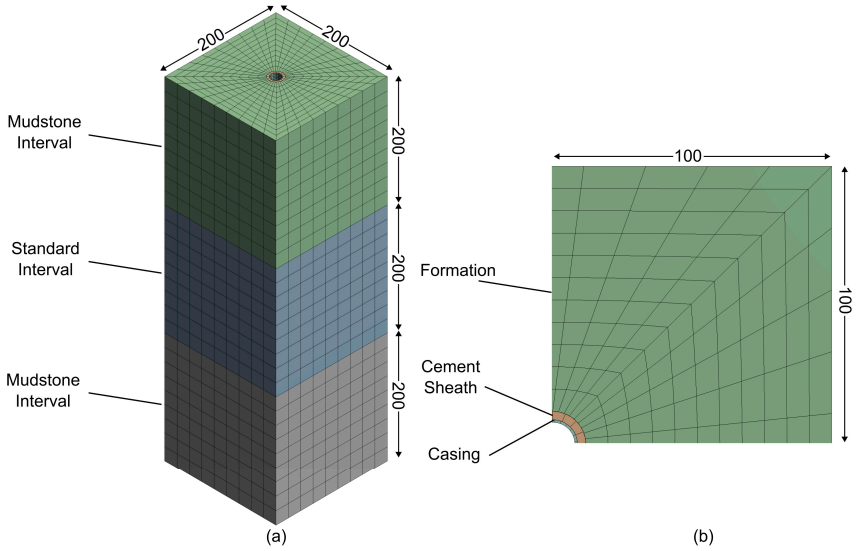


Figure 3. Mechanical analysis model of the casing–cement sheath-formation system, (**a**) Three-dimensional finite element model and (**b**) Quarter cross-sectional model.

The model employs the J-55 casing type used in the study area, characterized by an outer diameter of 17.78 cm and a wall thickness of 0.92 cm. The cement sheath is modeled with a thickness of 3 cm, while the formation domain measures 200 cm by 200 cm by 600 cm and is vertically stratified into an upper mudstone interval, a marker interval, and a lower mudstone interval. All components—the casing, cement sheath, and formation—are assumed to behave as continuous elastic materials. Furthermore, the cement sheath is considered to be perfectly bonded to both the casing and the formation, preventing any relative slip at the interfaces and thereby ensuring displacement continuity across these boundaries.

The core water absorption experiment demonstrates that upon immersion in water, the mechanical properties of mudstone such as compressive strength, shear strength, and tensile strength obtained from natural immersion tests decline significantly as water content increases. As shown in Figure 4, three sample experimental results reveal that the water content of the mudstone follows a characteristic nonlinear progression over time, indicating that shear strength is more sensitive to water content. Additional assessments were conducted to evaluate the variation of several physical parameters of mudstone at different water contents, including bulk modulus, shear modulus, tensile strength, cohesion, and internal friction angle. The fitting equations, fitting accuracy, and applicable ranges are listed in Table 1.

Table 1. Fitting equations for water content-dependent mudstone parameters.

Parameter	Data Source	Fitting Equation	R^2	RMSE	Applicable Range
Water content	Natural immersion test	$\omega(t) = -0.005924t^2 + 0.291t + 0.3344$	0.9892	0.1099	3–24 days
Compressive strength		$\sigma_c(\omega) = -1.054\omega^2 - 3.732\omega + 43.34$	0.9997	0.1471	0.5–3.5%
Shear strength		$\tau(\omega) = -0.6717\omega^2 - 1.997\omega + 19.51$	0.9996	0.0991	
Bulk modulus	Controlled humidity test	$K(\omega) = 5179\omega^{-1.535}$	0.8952	186.4976	2–8%
Shear modulus		$G(\omega) = 8912\omega^{-1.823}$	0.9270	216.5372	
Tensile strength		$\sigma_t(\omega) = -0.4363\omega + 4.189$	0.9989	0.0269	
Cohesion		$c(\omega) = -1.801\omega + 15.01$	0.9972	0.1774	
Internal friction angle		$\phi(\omega) = -2.231\omega + 30.62$	0.9964	0.2493	

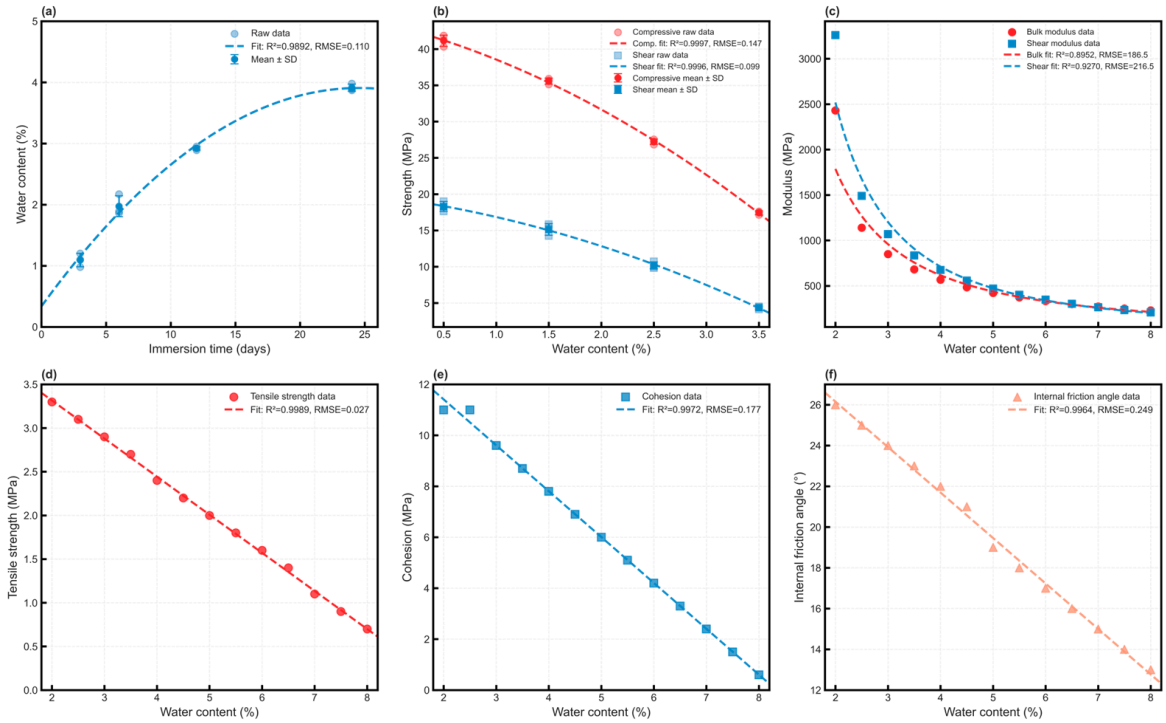


Figure 4. Relationships between water content and mudstone mechanical properties. Panels (**a**,**b**) are based on natural immersion tests (mean ± SD, n = 3) covering 0–4% water content. Due to the extremely low permeability of mudstone and specimen disintegration during prolonged immersion, these tests were limited to the low water content range; Panels (**c**–**f**) are based on controlled-humidity tests, which extended the characterization of mechanical parameters to the water content range of 2–8%. Dashed lines represent the fitted relationships, with the corresponding R^2 and RMSE values shown in the legends.

All these parameters exhibit a significant decreasing trend, corroborating the findings from the soaking experiments. When the water content reaches approximately 8%, the mudstone essentially loses its mechanical integrity, making it highly susceptible to fracturing under external stress. By comprehensively analyzing the material data from the oilfield and the core immersion experiment data, the parameters of different materials in the model are shown in Table 2, including the casing, cement sheath, marker interval, and mudstone.

Table 2. Parameters of materials in the numerical model.

Material Type	Water Content (%)	Density (kg/m^3)	Elastic Modulus (MPa)	Possion's Ratio	Tensile Strength (MPa)	Cohesion (MPa)	Internal Friction Angle (°)	Porosity
Casing (J-55)	/	7850	2.08×10^5	0.28	2.5×10^3	/	/	/
Cement sheath	/	1950	7×10^3	0.2	1	5	25	/
Marker interval	/	2020	6.69×10^3	0.158	2.43	8.3	28	0.15
Mudstone interval	2%	2200	6.75×10^3	0.03	3.3	11.4	25.78	0.08
	3%	2200	2.26×10^3	0.05	2.87	9.6	23.67	0.075
	4%	2200	1.44×10^3	0.07	2.43	7.8	21.56	0.07
	5%	2200	1.02×10^3	0.09	2	6	19.45	0.068
	8%	2200	478	0.15	0.7	0.6	13.12	0.067

The initial condition of the model is determined solely by gravity and the weight of the overlying rock layers, with the pressure from these layers calculated based on the burial depth of the strata. To simulate a semi-infinite formation, fixed boundary conditions are applied to the top and bottom surfaces, while normal displacement constraints are imposed

on the sides. Both ends of the casing and cement sheath are fixed in place. During the simulation, the water content at the mudstone boundary is varied to replicate the water injection process, enabling the calculation of water content distribution at various points within the formation. A constant water injection pressure of 11.5 MPa is applied to induce shear deformation in the casing, while water content results are incorporated as strain source terms related to mudstone hydration in the mechanical model.

5. Analysis and Discussion

Using the developed finite element model, the water content at the mudstone boundary is gradually increased from 2% to 8% to simulate its distribution throughout the formation. The results quantify the influence of water content on shear strain in each system component. Distinct behaviors at lithological interfaces reveal the fundamental cause of casing failure under these conditions.

5.1. Shear Strain Evolution at Lithological Interfaces

Due to mechanical property contrasts between the mudstone intervals and the marker interval within the N_2 section, shear strain at the lithological interface varies significantly with water content. Simulation results show three evolutionary stages: low (2–3%), moderate (4–5%), and high (8%) water content.

At 2% water content, shear strain in the marker interval concentrates near the wellbore, forming a localized high-strain zone, while the remaining region remains uniform, indicating stable behavior. In the mudstone interval, strain gradually increases along the water injection path, with a ring-shaped concentration around the wellbore and a higher gradient on the inflow side, reflecting stronger shear stress in that direction, as shown in Figure 5a,b.

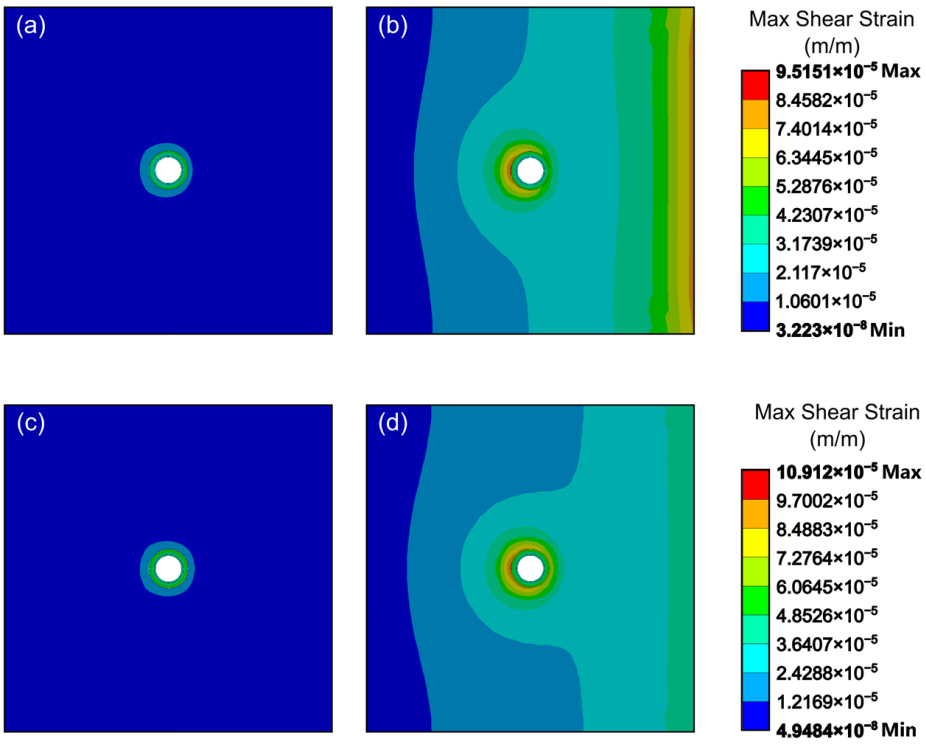


Figure 5. Maximum shear strain distribution at the lithological interface at water contents of 2% and 3% (low water content stage): (**a**) marker interval at 2%; (**b**) mudstone interval at 2%; (**c**) marker interval at 3%; (**d**) mudstone interval at 3%.

While water content increased from 2% to 3%, the shear strain response across all components is elevated overall. The marker interval maintains a localized high-strain zone near the wellbore but remains otherwise uniform. Maximum shear strain at model boundaries decreases slightly, whereas the mudstone interval develops a more distinct ring-shaped concentration around the wellbore, as illustrated in Figure 5c,d.

When the water content increases to 4%, there is a general rise in the maximum shear strain values across all model components, accompanied by a more intense distribution of responses and an expansion of the affected area. Figure 6a shows a modest enlargement of the localized high-strain zone near the wellbore within the marker interval, indicating progressive hydration effects. Simultaneously, mechanical properties of the mudstone interval deteriorate rapidly—elastic modulus, tensile strength, and cohesion drop markedly. Consequently, boundary strain values decline, while the ring-shaped strain localization around the wellbore becomes more prominent with an expanded high-strain region. This transition is attributed to the coupling of mudstone swelling and mechanical deterioration. As water injection continues, water content variability within the mudstone interval decreases, leading to a more uniform swelling response. Concurrently, when water content reaches 4%, rock strength declines significantly, reducing the mudstone's sensitivity to shear strain and facilitating strain localization in specific areas.

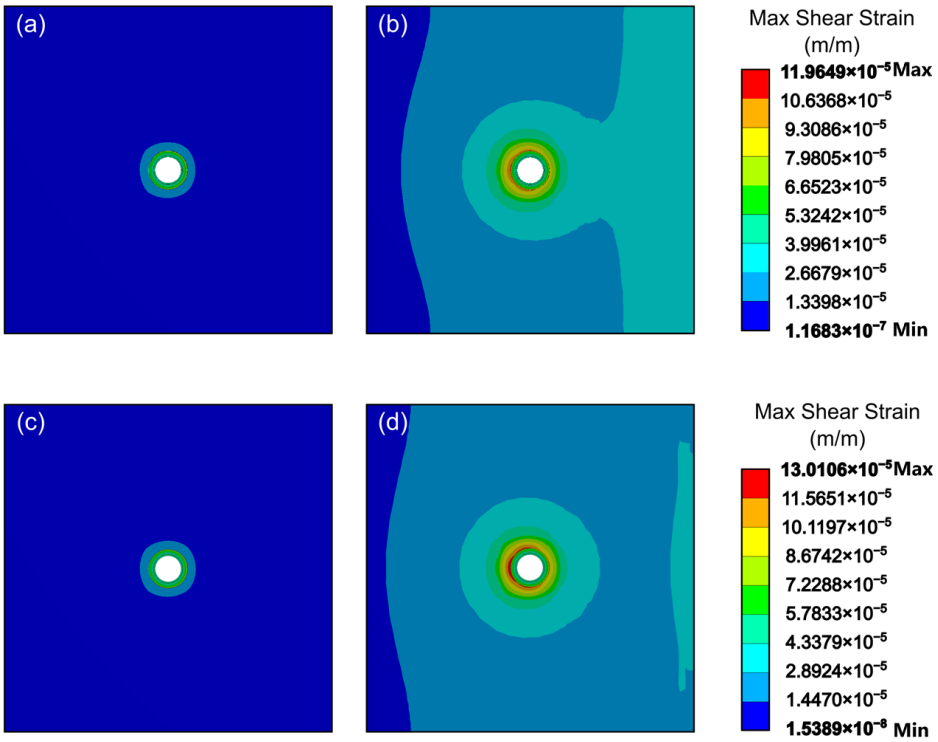


Figure 6. Maximum shear strain distribution at the lithological interface at water contents of 4% and 5% (moderate water content stage): (**a**) marker interval at 4%; (**b**) mudstone interval at 4%; (**c**) marker interval at 5%; (**d**) mudstone interval at 5%.

When the water content of the mudstone increases to 5%, the model's overall maximum shear strain value rises further, accompanied by a more pronounced localization. The marker interval, being insensitive to water immersion, maintains a relatively uniform distribution across most regions. In contrast, although the mudstone interval also exhibits a certain degree of uniformity, shear strain at the model boundaries decreases further, while a ring-shaped concentration around the wellbore expands with higher strain values, as shown in Figure 6c,d.

When the mudstone water content reaches 8%, the water content at each node tends to equilibrate, leading to the cessation of water-induced deterioration and stabilization of the mudstone mechanical properties, which become spatially uniform, as shown in Figure 7. The mudstone interval no longer contains weak zones caused by water content gradients. Shear strain around the borehole remains ring-shaped, gradually diminishing outward. All components exhibit ring-shaped shear strain localization, the most typical instability mode under axisymmetric conditions [29], with microcrack initiation likely along the direction of maximum shear stress.

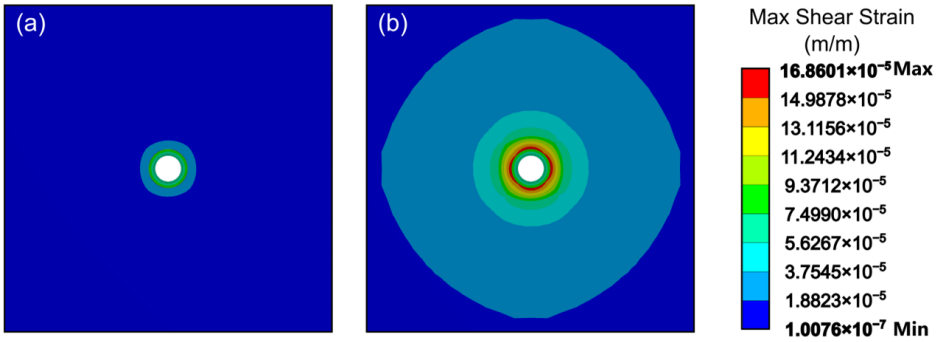


Figure 7. Maximum shear strain distribution at the lithological interface at water content of 8% (high water content stage): (**a**) marker interval at 8%; (**b**) mudstone interval at 8%.

The observed ring-shaped localization tendency can be attributed to the combined effects of mudstone mechanical parameter degradation, deformation compatibility, and the cylindrical geometry of the wellbore. As the bulk modulus, shear modulus, and shear resistance of the mudstone decrease, deformation incompatibilities arise among the weakened mudstone interval, the marker interval, the cement sheath, and the casing. Due to the constraints on relative displacement at the interfaces between these components, such incompatibilities are transformed into localized shear deformation near the wellbore and at lithological interfaces. The cylindrical geometry of the wellbore further promotes circumferential strain transfer, making high-strain zones more likely to concentrate around the wellbore under high water content conditions.

5.2. Localization Pattern in the Casing–Cement Sheath System

The disparity in maximum shear stress between the mudstone interval and the marker interval is subsequently transmitted to the casing–cement sheath system, as illustrated in Figure 8. Axially, the cement sheath exhibits a highly non-uniform shear strain, with multiple high-strain zones at lithological interfaces. The localized strain values in these zones approach the peak values of the mudstone interval itself, indicating that the cement sheath at this interface undergoes substantial shear deformation. Conversely, casing shear strain is generally lower and more uniformly distributed, following a pattern of lower within the marker interval, higher in the mudstone sections above and below.

Due to horizontal variations in water content influenced by flow direction, shear strain was analyzed along the x-direction (perpendicular to flow) and z-direction (parallel to flow). The evolution can be divided into three water content stages: low (2–3%), moderate (4–5%), and high (8%).

As shown in Figure 9, both casing and cement sheath exhibit elevated strain at ends and reduced strain in the middle along the x-axis, consistent with mudstone water softening. During the stage characterized by low water content (2–3%), strain values remain relatively minimal, indicating system stability; strain at ends is 4.63×10^{-5} (casing) and 5.11×10^{-5} (cement sheath), respectively. While water content rises to 8%, casing end strain rises by 15.8% to 5.36×10^{-5}, while cement sheath strain increases by 91.4% to

9.78×10^{-5}. At the mudstone-marker interface (dashed line in Figure 9), a distinct reversal in the shear strain gradient is observed. As detailed in Table 3, within the depth interval from 1.875 to 2 m, the strain gradient of the system is positive; however, it becomes negative from 2 to 2.125 m. This abrupt change in gradient confirms the presence of strain concentration effects induced by the lithological interface, causing a redistribution of shear stress within the system.

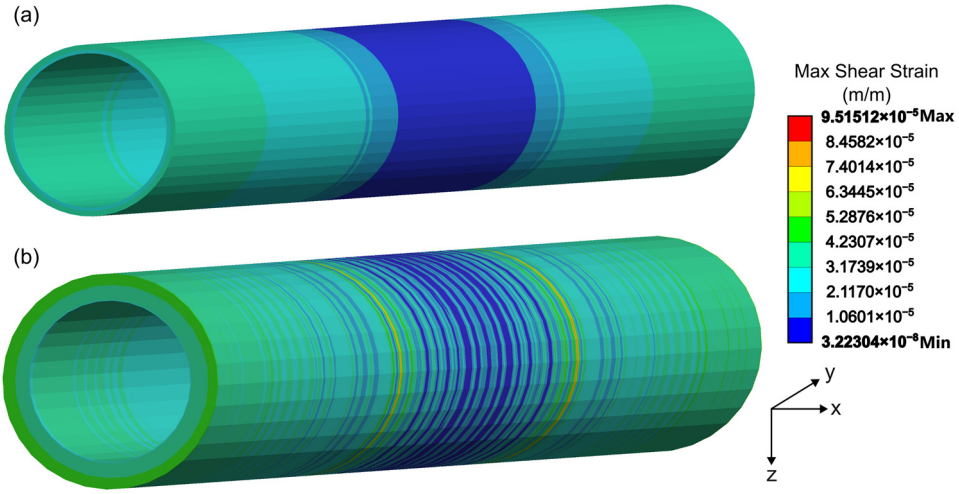


Figure 8. Distribution of maximum shear strain in the casing–cement sheath system: (**a**) casing and (**b**) cement sheath.

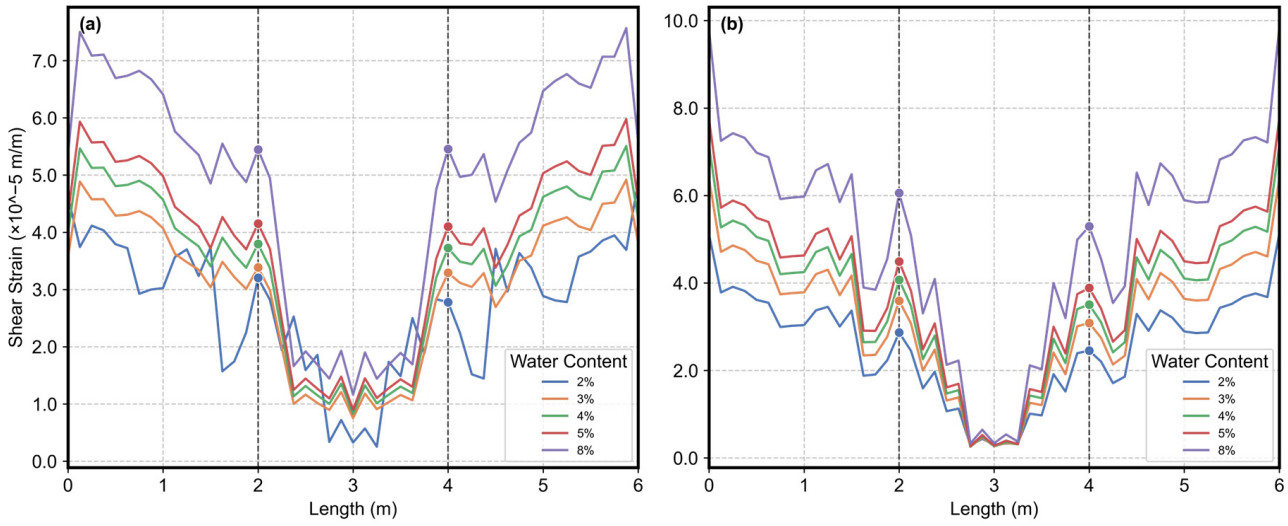


Figure 9. Maximum shear strain along the x-direction in the casing–cement sheath system: (**a**) casing and (**b**) cement sheath.

Table 3. Comparison of strain gradients in the x-direction of the casing–cement sheath system at the lithological interface.

Water Content	Strain Gradients of Casing ($\times 10^{-4}$ m/m)		Strain Gradients of Cement Sheath ($\times 10^{-4}$ m/m)	
	1.875 m–2 m	2 m–2.125 m	1.875 m–2 m	2 m–2.125 m
2%	7.60	−3.04	5.12	−3.36
3%	3.04	−3.20	6.56	−4.16
4%	3.36	−3.36	7.60	−4.80
5%	3.60	−3.52	8.56	−5.36
8%	4.56	−4.00	12.10	−7.76

Figure 10 illustrates that the shear strain distribution of the casing–cement sheath system exhibits a similar characteristic pattern along the z-axis, while strain coordination between casing and cement sheath differs due to seepage direction. At the critical interface, the casing exhibits a negative strain gradient (indicating strain reduction), whereas the cement sheath shows a positive gradient (indicating strain increase). The opposing signs of these gradients indicate strain incompatibility along this axis, which may be associated with interface debonding or relative slip.

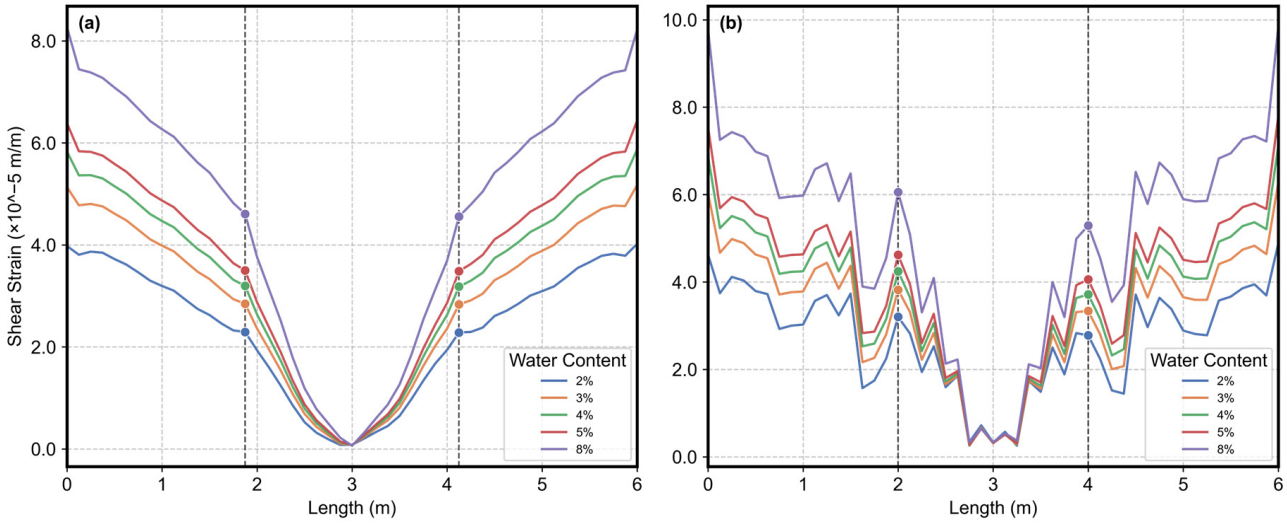


Figure 10. Maximum shear strain along the z-direction in the casing−cement sheath system: (**a**) casing and (**b**) cement sheath.

Despite the observed discrepancies in the shear strain trajectories of the casing–cement sheath system, the cement sheath continues to perform a crucial protective function. Under water content of 2%, cement sheath strain near the lithological interface increases sharply from 2.25×10^{-5} to 3.20×10^{-5}, while casing strain decreases from 2.29×10^{-5} to 1.93×10^{-5}. This behavior indicates that the cement sheath effectively buffers the casing, shifting casing stress concentrations slightly toward the ends. Although no gradient reversal occurs in the z-direction, the casing strain gradient changes rapidly near the interface as shown in Table 4.

Table 4. Comparison of casing strain gradients near the lithological interface.

Water Content	Strain Gradients of Casing ($\times 10^{-4}$ m/m)	
	1.75 m–1.875 m	**1.875 m–2 m**
2%	−0.24	−2.88
3%	−0.80	−3.84
4%	−0.96	−4.48
5%	−1.12	−4.96
8%	−1.68	−6.80

The cement sheath, known for its relative brittleness, serves as a critical stabilizing element for the wellbore but is consequently more susceptible to shear deformation. Simulation results reveal a significant increase in shear strain correlated with elevated water content. Although the strain levels remain below the yield threshold of the J-55 casing, the cumulative failure from sustained water injection and the potential for brittle fracture of the cement sheath warrant serious consideration. Failure of the cement sheath would lead

to an immediate increase in stress concentration on the casing, thereby substantially raising its risk of failure.

5.3. Field Comparison and Evidence for the Casing Failure Mechanism

The numerical results reveals that the hydration-induced degradation of the mechanical parameters of mudstone promotes localized shear deformation within the casing–cement sheath-formation system. To further correlate the numerical results with field observations, this study comprehensively analyzed the fault distribution and casing failure records in the study area. Two principal prerequisites are considered essential for the occurrence of casing failure in the N_2 section.

The first critical prerequisite is that the injection of high-pressure water into the reservoir units beneath the N_2 section. Notably, the N_2 section itself is not the direct target of the water injection; rather, it serves as the receiving interval affected by upward water migration and pressure transmission from the underlying reservoir units. Continuous high-pressure water injection provides the driving force for the local pore pressure field variation and subsequent mudstone hydration response. The other essential prerequisite is the presence of a complex, interconnected fault system providing effective pathways for the cross-interval movement of deep, high-pressure fluids from the reservoir units to the overlying mudstone interval of N_2 section [30].

Field observations support these two prerequisites. Figure 11a shows the spatial distribution of casing failure wells in the N_2 section in 2015, 2017, and 2019. Failures predominantly cluster around the periphery of the fault structural belt, exhibiting a gradual expansion from localized to a extended affected area. In 2015, the casing failure wells were mainly concentrated in the pinching zone between faults F164 and F167 and to the north of fault F1552, indicating early stress propagation along the fault belt. After 2018, the number of casing failure increased markedly, with new clusters near fault F167 extending toward fault F157. This transition signifies a shift from localized to regional geostress disturbance, underscoring the controlling influence of faults.

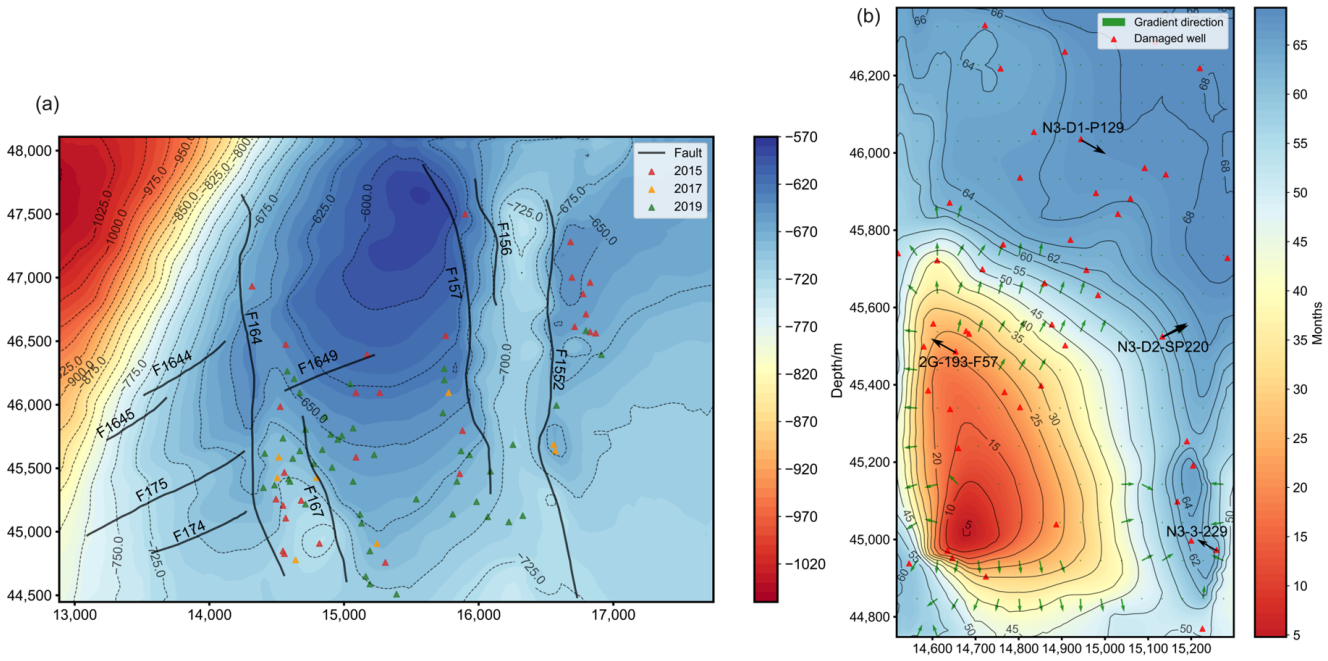


Figure 11. Casing failure observation results in the N_2 member: (**a**) Faults and casing failure well locations, and (**b**) Casing failure gradient analysis in the area affected by the F167 fault.

Moreover, if the injected water serves as the primary driving force responsible for inducing casing failure, the migration pathway of the injected water should spatially correspond with the occurrence and propagation of casing failure. Figure 11b presents quantitatively the typical propagation direction of casing failure diffusion in the area affected by fault F167, based on the timing of casing failure events and well locations. The findings indicate that the diffusion rate is highest within 10 to 20 months after the initial casing failure, reaching a maximum velocity of approximately 35 m per month. The gradient direction is denoted by the green arrow in Figure 11b. Wellbore logging data from the F164 fault area determined collapse orientations, identifying the stress direction associated with the casing failure (represented by black arrows in Figure 11b). For well 2G-193-F57, stress direction is NW117.0°, aligning with the calculated gradient direction. Well N3-3-229 shows the same orientation. Minor variations exist for wells N3-D1-P129 and N3-D2-SP220, but measured directions generally concur with the gradient direction. These observations indicate that the fault-controlled migration pathway and the deformation response of casing failure wells exhibit a consistent spatial trend.

Based on wellbore logging data, casing diameter changes and failure interval statistics provide another quantitative field evidence of casing deformation in the N_2 section. As shown in Figure 12a, casing diameter changes in marker interval and lower interval are mainly concentrated in large diameter change ranges, indicating that the casing in these intervals experienced a strong mechanical response and high-intensity non-uniform external loading. Figure 12b further shows that casing failure wells are predominantly concentrated in the marker interval and lower interval, which together account for more than 90% of the casing failure wells in the N_2 section. The prominent occurrence of casing failure in the lower interval is consistent with the upward migration of injected water and pressure from the underlying reservoir units through fault-controlled pathways. The concentration of failure in the N_2 marker interval further indicates that the migrated water and pressure tend to induce stronger mechanical responses near mudstone intervals and lithological interfaces.

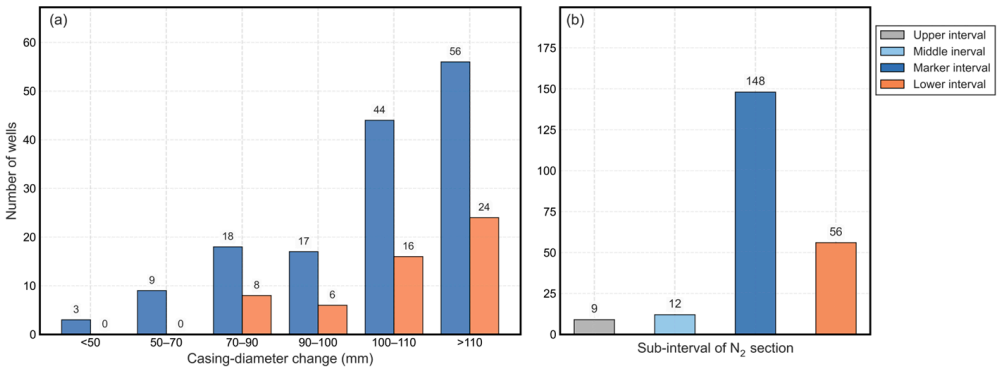


Figure 12. Quantitative field evidence of casing deformation in the N_2 section. (**a**) Distribution of casing diameter changes in the marker interval and lower interval of the N_2 section. (**b**) Distribution of casing failure wells among different N_2 sub-intervals.

The field observations are consistent with the numerical results in terms of stratigraphic concentration and mechanical response characteristics. These results support a casing failure mechanism in which high-pressure water injection provides the driving force, fault-controlled upward water pressure transmission affects the N_2 interval, mudstone hydration weakens the responsive interval, and interface-related deformation promotes casing failure. Based on the agreement between field observations and numerical results, the casing failure mechanism in the N_2 section can be summarized into five sequential stages, as shown in Figure 13.

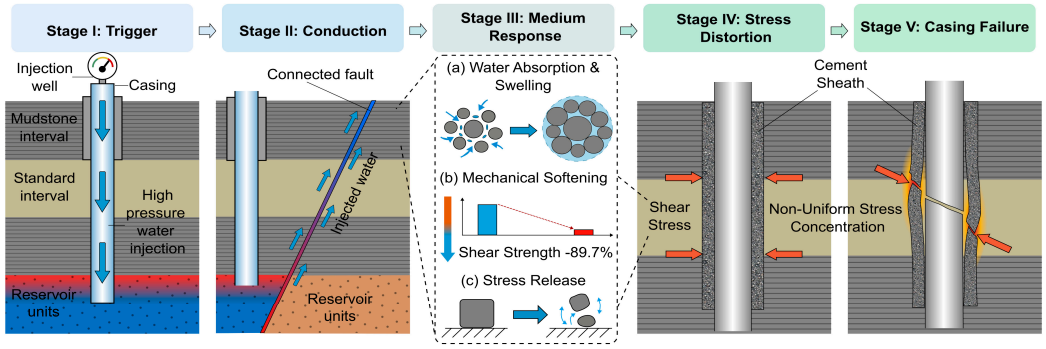


Figure 13. Schematic diagram of the evolution process of casing failure mechanism.

1. Trigger Stage: injecting high-pressure water into the reservoir units;

High-pressure water injection maintains elevated formation pressure within the reservoir units, creating a stable, high-pressure energy reservoir. During this stage, the N_2 section, which is not directly subjected to water injection, remains unaffected and maintains a state of stress equilibrium.

2. Conduction Stage: propagation of pressure and fluid through the fault network;

Interconnected faults facilitate the transfer of high-pressure fluids and pressure from the reservoir units to the mudstone interval of N_2 section. The connectivity of these fault channels ensures the efficient transmission of both energy and fluids, making the N_2 section the direct recipient of the water injection effect.

3. Medium Response Stage: three-stage synergistic deterioration following water absorption in mudstone;

Upon exposure to high-pressure fluid, the mudstone in the N_2 section undergoes a series of synergistic processes: water absorption and swelling, wherein hydration of mudstone particles causes a marked increase in water content, structural loosening, and subsequent volume expansion; mechanical softening, whereby shear strength decreases by approximately 89.7% relative to its original state, significantly reducing load-bearing capacity; and stress release, during which volumetric expansion disrupts the intrinsic stress equilibrium, resulting in stress relaxation. These three phases—swelling, softening, and stress release—constitute the core of the medium's response and play a pivotal, synergistic role in inducing casing failure.

4. Stress Distortion Stage: development of heterogeneous shear stress localization;

The processes of swelling, softening, and stress release in the mudstone disrupt the original stress equilibrium within the formation, creating a heterogeneous stress field. The mechanically weakened mudstone cannot distribute stress uniformly, leading to localized stress concentrations around the casing.

5. Casing Failure Stage: Shear failure of the casing−cement sheath system occurs;

While the shear stress localization around the casing exceeds the shear strength threshold of the casing−cement sheath system, the casing initially undergoes deformation, followed by shear fracture, ultimately leading to casing failure.

Although the above field observations and numerical results provide a consistent explanation for the casing failure mechanism in the N_2 section, the interpretation should be considered within the assumptions of the present model. The one-way coupling approach does not account for the feedback of deformation-induced changes in pore structure and hydraulic conductivity on the seepage process. Such feedback may become more significant under high water content conditions and may influence the subsequent redistribution of water. Therefore, the present results are interpreted primarily in terms of the evolution

trend and spatial characteristics of shear−strain localization within the casing–cement sheath-formation system. A two-way hydromechanical coupling approach should be considered in future studies to further evaluate the interaction between water migration and deformation under strong hydration conditions.

6. Conclusions

This research employs a three-dimensional fluid–solid coupling numerical model to systematically investigate the strain evolution and localization behavior within the casing–cement sheath-formation system subjected to mudstone hydration. The main conclusions are as follows:

The nonlinear degradation of mudstone mechanical properties with increasing water content is the primary mechanism driving casing failure. Specifically, as water content rises from 2% to 8%, the mudstone's shear strength decreases by 89.7%, while its elastic modulus declines by more than two orders of magnitude. Among the mechanical parameters evaluated, shear strength shows the greatest sensitivity to changes in water content.

As water content increases, the pattern of shear strain evolution distinctly transitions from a discrete distribution to annular localization. At low water content levels (2–3%), shear strain concentrates discretely near the wellbore and along the direction of water injection. At moderate water content (4–5%), this concentration evolves into an annular configuration with an expanded high-strain zone. When water content reaches 8%, a fully developed annular shear band centered on the wellbore emerges, representing a characteristic precursor to instability under axisymmetric conditions.

The axial shear strain distribution within the casing exhibits a pattern characterized by low strain in the central section and high strain at both ends, with the lithological interface identified as the most critical risk zone. Notably, the strain increase observed in the cement sheath—up to 91.4%—is substantially greater than that in the casing. A pronounced reversal in the strain gradient occurs at the interface between the mudstone and the marker layer, confirming that mechanical discontinuities at lithological boundaries induce shear stress redistribution, thereby making these interfaces the system's weakest points.

The analysis of the evolution of casing failure mechanisms reveals that injection pressure and mudstone water content jointly govern the development of casing failure. Consequently, strategies aimed at reducing injection pressure and mitigating increases in mudstone water content are effective in decreasing the risk of casing failure. This study provides theoretical insights that support the prediction and prevention of casing failure in oilfields developed through water injection. The proposed mechanism and analytical procedure are particularly relevant to waterflooded fault-block reservoirs, where injection-induced pressure transmission, water-sensitive mudstone or shale intervals, and non-uniform deformation near lithological interfaces coexist. When applied to other geological systems, material parameters, stress conditions, and injection-related settings should be determined based on local geological and engineering data.

Author Contributions: Conceptualization, K.Z. and F.M.; Methodology, K.Z. and T.Y.; Software, T.Y., Z.L. and X.Z.; Formal Analysis, K.Z. and T.Y.; Validation, T.Y., Z.L. and X.Z.; Visualization, K.Z. and T.J.; Writing—Original Draft Preparation, K.Z. and T.J.; Writing—Review & Editing, K.Z., F.M., T.Y. and X.Z.; Resources, F.M.; Supervision, F.M.; Project Administration, F.M.; Funding Acquisition, F.M. and Z.L. All authors have read and agreed to the published version of the manuscript.

Funding: This work was funded by the National Natural Science Foundation of China, grant number 41174157, and 42304111; and the Natural Science Foundation of Shandong Province, grant number ZR2022QD067, and ZR2022QD076.

Data Availability Statement: Non-sensitive data that are unrelated to routine field operations may be made available from the corresponding author upon reasonable request. Sensitive casing failure data cannot be disclosed due to confidentiality agreements related to oilfield operation.

Conflicts of Interest: The authors declare no conflicts of interest.

References

1. Lu, Y.; Wang, L.; Sun, X.; Wang, J. Experimental study of the influence of water and temperature on the mechanical behavior of mudstone and sandstone. *Bull. Eng. Geol. Environ.* **2016**, *76*, 645–660. [CrossRef]
2. Chen, F.; Sun, X.; Lu, H. Influence of water content on the mechanical characteristics of mudstone with high smectite content. *Geofluids* **2022**, *2022*, 9855213. [CrossRef]
3. Zhang, N.; Wang, H.; Wang, S.; Wang, S.; Guo, Y.; Xun, X. Study on the evolution law of pore structure and mechanical properties of mudstone under the effect of water-rock chemistry. *J. Porous Media* **2023**, *26*, 1–22. [CrossRef]
4. Geng, J.; Sun, Q.; Li, H.; Yang, Y. Deterioration of mudstone exposed to cyclic hygrothermal conditions based on thermoacoustic emission. *Constr. Build. Mater.* **2023**, *386*, 131581. [CrossRef]
5. Li, G.; Jiang, Z.; Feng, X.; Zhang, N.; Xu, X. Relation between molecular structure of smectite and liquefaction of mudstone. *RSC Adv.* **2015**, *5*, 23481–23488. [CrossRef]
6. Guan, H.; Ren, Y.; Ling, S.; Wu, X.; Yu, T.; Li, X.; Wang, S.; Sun, C. Microstructure and water-swelling mechanism of red-bed mudstone in the Xining region, northeastern Tibetan Plateau. *J. Rock Mech. Geotech. Eng.* **2024**, *16*, 2537–2551. [CrossRef]
7. Zhang, H.; Hou, B.; Yin, G.Q.; Chen, M.; Li, C.; Jin, Y.; Yuan, F. The damage and deformation mechanism of soft mudstone in drilling engineering. *Adv. Mater. Res.* **2012**, *524–527*, 1610–1614. [CrossRef]
8. Wang, T.; Yan, C. Investigating the influence of water on swelling deformation and mechanical behavior of mudstone considering water softening effect. *Eng. Geol.* **2023**, *318*, 107102. [CrossRef]
9. Gao, Y.; Wei, W.; Jiang, Q. Effect of water content on mechanical properties and internal microcrack evolution in mudstone. *Arab. J. Sci. Eng.* **2022**, *48*, 12775–12791. [CrossRef]
10. Liu, C.D.; Cheng, Y.; Jiao, Y.Y.; Zhang, G.H.; Zhang, W.S.; Ou, G.Z.; Tan, F. Experimental study on the effect of water on mechanical properties of swelling mudstone. *Eng. Geol.* **2021**, *295*, 106448. [CrossRef]
11. Huang, K.; Dai, Z.; Yan, C.; Chen, S. Numerical study on the swelling and failure of red-layer mudstone subgrade caused by humidity diffusion. *Comput. Geotech.* **2023**, *156*, 105272. [CrossRef]
12. Zhang, C.L.; Wieczorek, K.; Xie, M.L. Swelling experiments on mudstones. *J. Rock Mech. Geotech. Eng.* **2010**, *2*, 44–51. [CrossRef]
13. Chang, Z.; Hou, B.; Wang, T.; Zhou, B. Casing damage mechanism from short-term water injection development in the Yingdong Oilfield. *Pet. Sci. Bull.* **2020**, *5*, 549–559. [CrossRef]
14. Chen, Z.; Zhu, W.; Di, Q. Elasticity solution for the casing under linear crustal stress. *Eng. Fail. Anal.* **2018**, *84*, 185–195. [CrossRef]
15. Yin, Y.Q.; Cai, Y.E.; Chen, Z.W.; Liu, J.S. Theoretical solution of casing loading in non-uniform ground stress field. *Acta Pet. Sin.* **2006**, *27*, 133–138. [CrossRef]
16. Guo, X.L.; Li, J.; Zeng, Y.J.; Ding, S.D.; Zhang, X. Analytical method to evaluate casing stress during multi-fracturing for shale gas wells. *Mater. Sci. Forum* **2019**, *944*, 1050–1060. [CrossRef]
17. Zhou, B.; Zhang, X.; Zhang, C.; Zhao, F. A semi-analytical method for the stress distribution around a borehole with multiple casings and cement sheaths. *Geoenergy Sci. Eng.* **2023**, *229*, 212091. [CrossRef]
18. Chen, Z.F.; Li, X.Y.; Wang, W.; Lu, K.Q.; Zhu, W.P. Theoretical analysis of casing collapse in locally expansive mudstone. *J. Pet. Sci. Eng.* **2021**, *203*, 108643. [CrossRef]
19. Zhang, R.; Zhang, B.; Cao, L.; Lu, N.; Xu, Y.; Wu, L.; Wang, S.; Jiang, R. Evaluation of the casing strength reliability in deep gas well by taking into account the cement quality and strength uncertainty: Method, analysis and application. *Geoenergy Sci. Eng.* **2024**, *234*, 212623. [CrossRef]
20. Wu, T.; Li, M.; Liu, N.; Zhang, T.; Su, J. Research on mechanism of non-uniform in-situ stress induced casing damage based on finite element analysis. *Appl. Sci.* **2024**, *14*, 5987. [CrossRef]
21. Zhu, X.; Sun, H.; Jing, J.; Xu, P.; Kong, L. Study of response pattern of casing under the condition of nonuniform creep loading of shale gas reservoir. *Processes* **2026**, *14*, 234. [CrossRef]
22. Li, Z.; Li, H.; Li, G.; Yu, H.; Jiang, Z.; Liu, H.; Hu, S.; Tang, B. The influence of shale swelling on casing deformation during hydraulic fracturing. *J. Pet. Sci. Eng.* **2021**, *205*, 108844. [CrossRef]
23. Li, H.; Li, Z.; Li, G.; Yu, H.; Jiang, Z.; He, L.; Guo, B.; Dong, M. Casing deformation mechanisms of horizontal wells in Weirong shale gas field during multistage hydraulic fracturing. *J. Nat. Gas Sci. Eng.* **2020**, *84*, 103646. [CrossRef]
24. Wang, F.; Ding, X.; Song, C.; Liu, D. A Novel Hydromechanical Coupling Constitutive Model for Jointed Rock Masses Informed by Compression–Shear–Seepage Tests. *Int. J. Geomech.* **2026**, *26*, 04026033. [CrossRef]

25. Gao, Y.; Xi, D.; Qin, Z.; Ma, P.; Wang, C. Clay mineralogy of the first and second members of the Nenjiang Formation, Songliao Basin: Implications for paleoenvironment in the Late Cretaceous. *Sci. China Earth Sci.* **2017**, *61*, 327–338. [CrossRef]
26. Biot, M. General theory of three-dimensional consolidation. *J. Appl. Phys.* **1941**, *12*, 155–164. [CrossRef]
27. van Genuchten, M.T. A closed-form equation for predicting the hydraulic conductivity of unsaturated soils. *Soil Sci. Soc. Am. J.* **1980**, *44*, 892–898. [CrossRef]
28. Timoshenko, S.; Goodier, J.N. *Theory of Elasticity*; McGraw-Hill: New York, NY, USA, 1951.
29. Lian, Z.; Luo, Z.; Yu, H.; Bu, H.; Li, C.; Li, C. Finite element analysis and control measures on casing failure in sand shale interbeds. *Oil Drill. Prod. Technol.* **2016**, *38*, 887–892. [CrossRef]
30. Lao, H.; Wang, Y.; Li, J.; Shan, Y.; Song, L. Normal fault transmissibility characteristics under the transition condition of fault conduction and sealing observed in simulation experiments. *Mar. Pet. Geol.* **2022**, *143*, 105779. [CrossRef]

Disclaimer/Publisher's Note: The statements, opinions and data contained in all publications are solely those of the individual author(s) and contributor(s) and not of MDPI and/or the editor(s). MDPI and/or the editor(s) disclaim responsibility for any injury to people or property resulting from any ideas, methods, instructions or products referred to in the content.